Chemical Science

ROYAL SOCIETY OF CHEMISTRY

EDGE ARTICLE

View Article Online
View Journal | View Issue

Check for updates

Cite this: *Chem. Sci.*, 2025, **16**, 10357

All publication charges for this article have been paid for by the Royal Society of Chemistry

Received 6th February 2025
Accepted 27th April 2025

DOI: 10.1039/d5sc00888c

rsc.li/chemical-science

Phase effect of TiO_2 on surface hydrogen adsorption/desorption in controlling photocatalytic methane conversion†

Jiakang You, [a] Ardeshir Baktash, [a] Dazhi Yao,[b] Yanzhao Zhang,[a] Shanshan Ding,[a] Jingwei Hou, [a] Guangyu Zhao,[b] Yonggang Jin,[b] Zhiliang Wang *[a] and Lianzhou Wang *[a]

Identifying the rate-determining step is crucial for designing an effective photocatalytic system. The surface adsorption/desorption behaviour of reactants has received much less attention in photocatalyst design because the charge separation and transfer in the bulk is commonly regarded as a more sluggish process. In this work, we investigate photocatalytic methane (CH_4) conversion (PMC) on various titanium oxide (TiO_2) surfaces, including rutile and anatase, and reveal that the influence of surface CH_4 adsorption can outweigh the photogenerated charge separation and transfer. Specifically, the rutile TiO_2 surface is totally inert for CH_4 activation. Further theoretical calculations reveal the significance of the hydrogen-adsorption/desorption process during the initial C–H bond cleavage on the TiO_2 surface. A reversible hydrogen adsorption/desorption process with a small Gibbs free energy not only enables the activation of the first C–H bond in CH_4 but also ensures a timely clearance of surface-adsorbed species, leading to a continuous PMC process. The findings of the phase effect study on the interaction between the photocatalyst surface and hydrogen atoms provide new insights into the rational design of efficient photocatalysts towards PMC. It also highlights the gap in transferring the knowledge of photocatalytic water splitting into PMC.

Photocatalytic methane conversion (PMC) has received increasing attention due to its potential to mitigate the greenhouse effect of methane (CH_4) and upgrade it into high-value products.[1–6] As an emerging research frontier, a comprehensive understanding of the photocatalyst design principle is critical for a highly selective and efficient PMC process. Currently, the knowledge from photocatalytic water splitting is used to guide photocatalyst design.[7–9] However, the PMC process is obviously different from the water-splitting system, making some of the knowledge accumulated from water-splitting reactions invalid.[10–13] There is a clear need to explore the key selection criteria for CH_4 conversion photocatalysts.

It is commonly known that photocatalysis is a complicated multi-step process, dominated by three key steps: light harvesting, charge separation and transfer (CST), and surface reaction.[14–18] Identifying the rate-determining step is crucial for designing an effective photocatalytic system. In the photocatalytic water splitting process, the CST efficiency generally bottlenecks the whole process.[19–21] Therefore, materials engineering has been implemented to create a higher CST driving force, with the surface properties of the photocatalysts being dramatically changed.[22–25] However, the majority of PMC studies are conducted in a gas–solid reaction system, making this process sensitive to the photocatalyst surface.[26] The experience from the conventional thermocatalytic CH_4 conversion process has recognized the significance of surface properties in methane activation.[27–29] Therefore, an in-depth understanding of how methane interacts with the photocatalyst surface will guide the future photocatalyst design for PMC.

The CH_4 molecule possesses high symmetric order, exhibiting a highly stable structure with strong C–H bonds.[30] Activating CH_4, *i.e.* scissoring the first C–H bond, is regarded as the most challenging step in the PMC process. Numerous researchers have reported that lattice oxygen plays a significant role in CH_4 activation, wherein CH_4 is cracked on the surface of metal oxide photocatalysts and C–C coupling occurs on the supported metal cocatalysts.[31–33] Despite the fact that many surface metal cocatalysts have been developed, only very limited metal oxides, including TiO_2 and ZnO, were reported to achieve a successful PMC process.[34–38] Taking the extensively studied TiO_2 as an example, various photoactive phases, including anatase, rutile, and brookite, have been reported to be active in

---

[a] Nanomaterials Centre, School of Chemical Engineering and Australian Institute for Bioengineering and Nanotechnology, The University of Queensland, St Lucia, Queensland, 4072, Australia. E-mail: zhiliang.wang@uq.edu.au; l.wang@uq.edu.au

[b] CSIRO Mineral Resources, 1 Technology Court, Pullenvale, QLD 4069, Australia

† Electronic supplementary information (ESI) available. See DOI: https://doi.org/10.1039/d5sc00888c

water splitting,[39–43] and the formation of mixed-phase junctions has been confirmed to be an effective strategy for CST improvement.[44–46] Nevertheless, current TiO_2-based photocatalysts for PMC reactions are dominated by the anatase phase,[2,47,48] while a fundamental understanding of the phase effect of photocatalysts on the interaction of CH_4 on the catalyst surface is still limited.

In this work, we investigate the CH_4 activation on different surfaces of TiO_2, including rutile and anatase, and discover that the rutile TiO_2 surface is completely inert for CH_4 activation. In comparison, the anatase TiO_2 exhibits a photocatalytic oxidative coupling of methane (POCM) to ethane (C_2H_6) activity of 2.1 mmol g^{-1} h^{-1}. Further investigations into the anatase/rutile mixed phase system indicate that the presence of rutile TiO_2 seriously deteriorates the CH_4 conversion despite the improved CST capability from the phase junction. Further theoretical calculation suggests that the behaviour of hydrogen (H) adsorption and desorption after the first C–H bond cleavage on TiO_2 plays a crucial role in the overall catalytic process. On rutile TiO_2, the H is strongly bonded to the surface and blocks the CH_4 activation pathway. In comparison, the H bonded to the anatase surface exhibits mild binding strength. Interestingly, it is discovered that the bond is sufficiently strong to activate CH_4 molecules, yet weak enough to be removed, thereby exposing active sites for the subsequent methane reaction. These findings highlight the surface sensitivity during methane activation and indicate that the H-adsorption strength is an important parameter in designing new photocatalysts for efficient methane conversion.

A series of TiO_2 photocatalysts containing different ratios of anatase and rutile phases were prepared *via* thermal annealing of commercial anatase TiO_2 nanoparticles (Fig. S1†) in the temperature range of 700–1000 °C in a muffle furnace (samples denoted as T-700–1000). Synchrotron-based X-ray diffraction (XRD) patterns (Fig. 1a and S2†) proved the gradual crystal phase transition from anatase to rutile. The XRD peaks at 25.3° and 27.4° correspond to anatase (101) and rutile (110) TiO_2, respectively,[49] based on which the ratio of these two phases is quantitatively determined (Table S1†). This indicates that the TiO_2 maintains the anatase phase below 700 °C, while the proportion of rutile TiO_2 increases with elevated temperature and is fully converted into rutile at 1000 °C. Raman spectral analysis further confirms this gradual crystal phase transition with Raman shifts at 398, 517 and 641 cm^{-1} corresponding to anatase, while the shifts at 449 and 611 cm^{-1} are assigned to rutile (Fig. 1b).[50,51]

To evaluate the methane conversion rate, the as-prepared TiO_2 photocatalysts were first loaded with gold (Au) nanoparticles as cocatalysts, which have been confirmed to be a good surface catalyst for ethane production.[32,52] The Au cocatalyst can enhance the C_2H_6 selectivity by facilitating the desorption of methyl species and suppressing CH_4 overoxidation to CO_2.[32,52] Inductively coupled plasma atomic emission spectroscopy (ICP-AES) confirms the Au amount to be around 3.8 wt% for all the samples. A stainless-steel flow reactor was used to evaluate the POCM performance with a flow rate of 126 mL min^{-1} (CH_4/O_2 gas ratio of 125/1) and a 300 W Xe lamp (full spectrum, Perfectlight Technology Co., Ltd) as the light source. As shown in Fig. 1c, T-700 shows an ethane production rate of 2.15 mmol g^{-1} h^{-1} together with a methane conversion rate of 5.60 mmol g^{-1} h^{-1}. The corresponding apparent quantum yield of methane conversion is 8.89% (±0.32%) at the wavelength of 350 nm (see

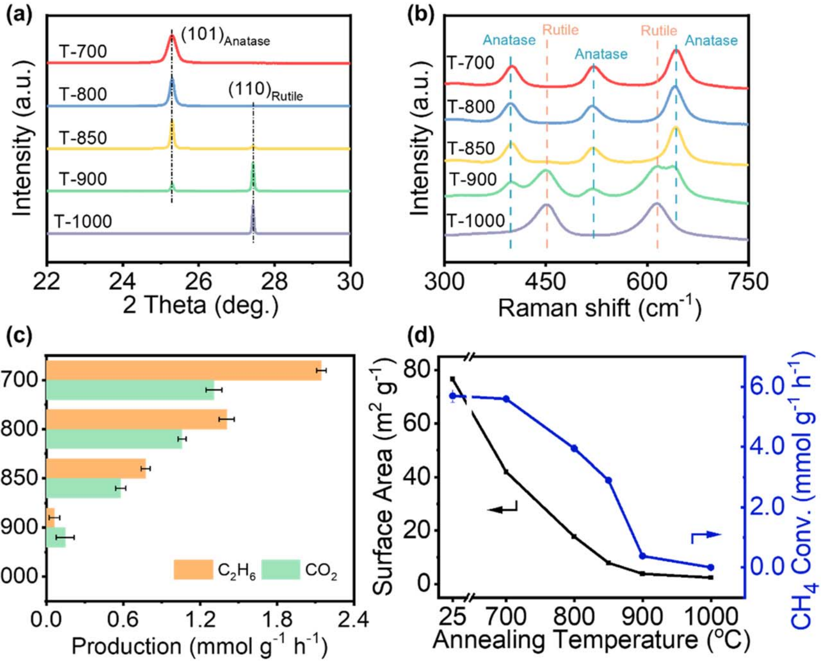

Fig. 1 The change in the TiO_2 photocatalyst at different temperatures (from 700 °C to 1000 °C), as determined from (a) XRD patterns and (b) Raman spectra. (c) POCM performance of different TiO_2-based photocatalysts (orange bar: C_2H_6; green bar: CO_2). (d) The CH_4 conversion rate (blue dot line) and the surface area change (black dot line) of different TiO_2-based photocatalysts prepared at different temperatures.

the ESI† for experimental details). Upon increasing the annealing temperature, a gradual decrease in the ethane production rate is observed. Eventually, when the sample is heated at 1000 °C, it shows no photoactivity at all. Meanwhile, a significant change in surface area is observed after the annealing process, as illustrated in Fig. 1d. As heating has changed several features (*i.e.*, phase and surface area) of TiO_2, we need to further study what dominated the key changes in the PMC process. Additionally, blank experiments were performed under identical conditions, with ultra-high-purity argon (Ar, 99.95%) used as the purge gas instead of CH_4. When Ar was employed in place of CH_4, no production of C_2H_6 was observed. This result confirms that the formation of C_2H_6 originates from the PMC. A long-term stability test was conducted using T-700, demonstrating stability over 20 hours (Fig. S3, see more discussion in Fig. S4†). These results safely exclude the impact of carbon contamination on PMC.[53,54]

Scanning electron microscopy (SEM) was conducted to observe the morphology of the as-prepared TiO_2-based photocatalysts. As shown in Fig. 2a, the particles start to sinter together when the annealing temperature increases over 800 °C. Further combining with the phase change results in Fig. 1a and d, it is revealed that large particles should possess the rutile phase with a reduced surface area. According to previous studies and our observations, during the phase transformation in TiO_2 nanoparticles, the rutile phase initially forms at the interfaces where anatase particles come into contact and undergo sintering (scheme in Fig. 2a).[55,56] UV-visible light absorption spectra reveal a slightly extended light absorption range with increased heating temperatures (Fig. 2b), corresponding to the phase transfer from anatase (3.18 eV) to rutile (2.98 eV).[57] We then applied the time-resolved photoluminescence (TRPL) decay to investigate the CST process of the photocatalysts. As shown in Fig. 2c and Table S2,† the formation of a mixed-phase junction extends the charge carrier lifetime from 1.54 ns to 7.65 ns. However, further increasing the rutile content leads to a reduction in the carrier lifetime to 4.49 ns for pure rutile TiO_2.

To analyze the correlation between light absorbance and CST with the CH_4 conversion rate ($r(CH_4)$), a Pearson Correlation Coefficient (PCC) analysis was performed (Table S3†). An absolute PCC value close to one indicates a strong correlation, while the sign of the value (positive or negative) indicates whether the correlation is positive or negative. It is generally accepted that extended light absorption ability and CST would benefit a photocatalytic process; therefore, we can expect a positive PCC if any of these two factors plays a determining role. Since the applied photocatalysts are loaded with Au nanoparticles, they show obvious localized surface plasmon resonance absorption at around 550 nm (Fig. S5†). However, the POCM test with a 420 nm cutoff filter shows no detectable product, which indicates that the LSPR effect cannot directly activate CH_4. Therefore, the light absorbance was calculated based on the pure TiO_2 samples (see the ESI† for calculation details). According to the light absorbance–$r(CH_4)$ relationship in Fig. 3a, the negative PCC (−0.95) means that better light harvesting will result in a worse performance, which is contradictory to the consensus of light harvesting influence on photocatalysis. This result suggests that light-harvesting is not the key feature in determining the CH_4 conversion rate.

Moreover, the PCC of $r(CH_4)$-τ is −0.47, indicating that the charge carrier lifetime is less determinative for the CH_4 conversion process. In particular, the 850 °C annealing treatment has extended the photocatalyst lifetime by 5 times but

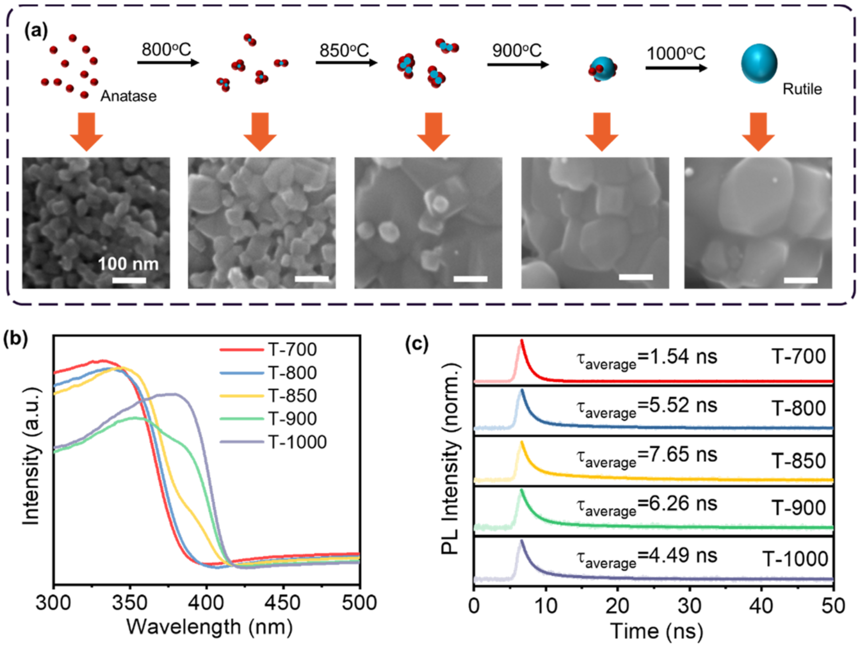

Fig. 2 (a) Schematic illustration of TiO_2 particle growth with the corresponding SEM images; (b) UV-vis spectra of commercial anatase annealed at different temperatures having different ratios of the rutile phase; (c) the TRPL decay curves of the as-prepared TiO_2 photocatalysts.

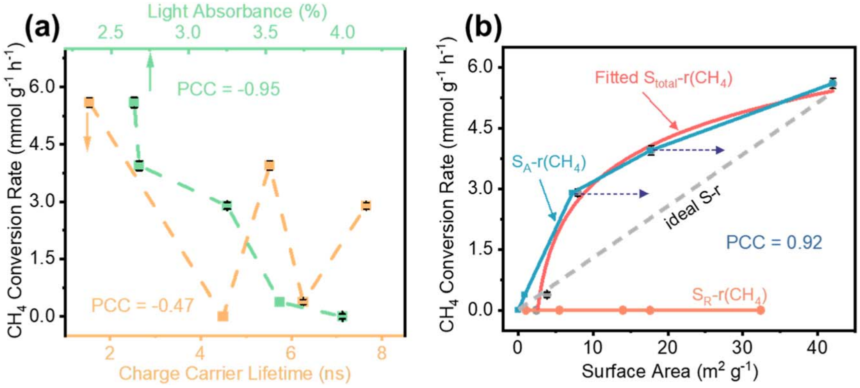

Fig. 3 CH_4 conversion rate ($r(CH_4)$) plotted against (a) the charge carrier lifetime (orange) and light absorbance (green) and (b) surface area.

reduced the CH_4 conversion rate by *ca.* 50% compared to the samples treated at 700 °C. This finding is significantly different from the knowledge of photocatalytic water splitting wherein a longer lifetime usually leads to a better performance.[58,59] Nevertheless, when taking the as-prepared samples for a photoelectrocatalytic water splitting test, it still shows that the sample with a longer lifetime (*e.g.*, T-850) possesses higher photocurrent density (Fig. S6†). The distinguishable performance dependence on carrier lifetime for water splitting and POCM indicates an unexplored mechanism during the POCM process.

Since the CH_4 reaction process occurs on the surface of catalysts in the gas phase, the surface area will play a critical role. We further analysed the change in the CH_4 conversion rate as a function of surface areas of the TiO_2 nanoparticles. As indicated in Fig. 3b, the surface area plays a significant role with a close correlation of the CH_4 conversion. Using the TiO_2 phase composition and surface area (S), a rough evaluation of the anatase surface area (S_A) can be conducted, assuming a uniform phase mixture. A strong correlation is observed between the two variables, S_A and $r(CH_4)$ (Fig. 3b, PCC = 0.92). When S_A exceeds a threshold, the $r(CH_4)$ exhibits a minimal change. For example, despite the pristine anatase TiO_2 having a much larger surface area than that of the 700 °C treated sample (retaining the anatase phase), they present nearly the same $r(CH_4)$, as shown in Fig. S7.† Meanwhile, according to previous studies, when phase transition happens in TiO_2 nanoparticles, the rutile phase first emerges at the interfaces when anatase particles are sintered.[55,56] It means that the majority of the TiO_2 surface remains as the anatase phase, despite the emergence of rutile inside the particles. Taking this into consideration, the S_A–$r(CH_4)$ relationship should closely resemble the ideal first-order reaction indicated by the grey dashed line in Fig. 3b. For comparison, we have prepared a series of rutile-based photocatalysts with different surface areas (see the ESI† for experimental details). None of these samples show POCM activity, as shown in Fig. 3b.

In particular, when comparing the rutile TiO_2 nanoparticle-based photocatalyst with the T-850 sample, even though the rutile sample shows a higher surface area (Table S4†) and similar particle size (Fig. S8†) and Au loading features (Fig. S9†), it is completely inactive for POCM (Fig. 3b). The strong dependence of $r(CH_4)$ on the anatase surface area and the nonactivity of rutile photocatalysts indicate that anatase is the only photoactive phase for methane activation. The surface properties play a more dominating role compared with the CST process, which is clearly different from the photocatalytic water splitting process. Considering that the anatase and rutile TiO_2 possess very similar features, it is worth further investigation on how such a tiny change can lead to a significant difference in methane activation.

Previous studies have revealed that methane activation starts from CH_4 cracking on the metal oxide surface with the participation of lattice oxygen.[60,61] Since oxygen can be consumed during methane activation, it will lead to the formation of oxygen vacancies (V_Os). We thus further applied *in situ* electron paramagnetic resonance (EPR) measurements to trace the V_O formation and investigate the interaction of CH_4 on the rutile and anatase surfaces. The EPR spectra for anatase- and rutile-based samples were measured under illumination without (Fig. S10a) and with (Fig. S10b†) methane (see the ESI† for experimental details). Methane activation dependence on different phases is revealed *via* the differential spectra shown in Fig. 4a. A significant increase of V_O ($g = 2.003$) and associated Ti^{3+} signals ($g = 1.98$) can be observed on anatase when exposed to a CH_4 atmosphere, wherein a much weaker V_O signal and undetectable Ti^{3+} signals are observed on the rutile phase. This result further confirms our hypothesis that CH_4 activation on anatase is much more favourable.

To acquire a deeper understanding of this methane activation process, a theoretical calculation on the first C–H bond activation with the following process (1) on rutile and anatase surfaces was performed:

$$CH_4 \rightarrow {}^*CH_4 \rightarrow {}^*H + CH_3 \tag{1}$$

where $^*CH_4$ represents the CH_4 adsorption on TiO_2, $^*H$ represents the H adsorption on TiO_2 and CH_3 represents the produced CH_3 groups. This free CH_3 group does not bond to the TiO_2 surface but instead diffuses onto the metal cocatalyst, as has been proposed in many previous studies.[32,33,62–65]

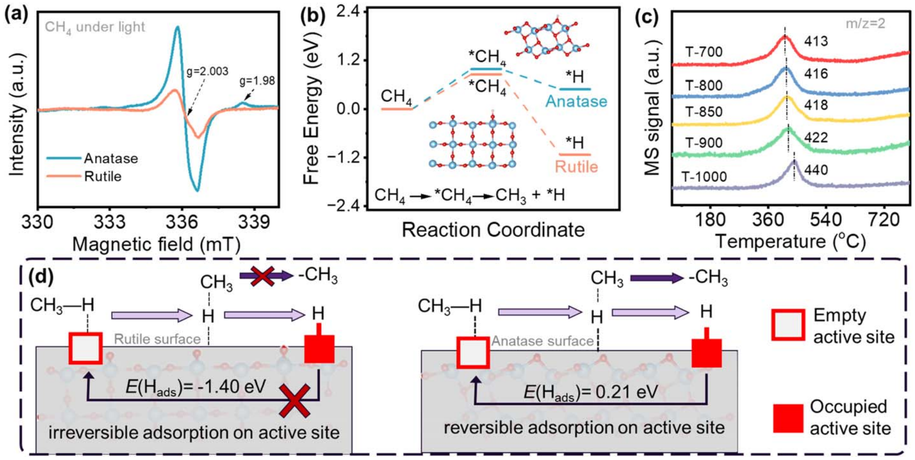

Fig. 4 (a) *In situ* EPR spectra of anatase and rutile; (b) computed Gibbs free energy of methane activation steps on anatase (101) and rutile (110) surfaces; (c) TPD-CH_4-MS spectra of as-prepared TiO_2 photocatalysts; (d) schematic illustration of surface adsorption behaviour of CH_4 on rutile and anatase, respectively.

In this theoretical calculation, Gibbs free energy is applied to evaluate this process at room temperature. The anatase (101) and rutile (110) surfaces are used for the calculation due to the significant diffraction peaks of these facets (Fig. 1a) and the widely accepted choice in previous research.[66–68] As shown in Fig. 4b, the Gibbs free energy is 0.49 eV on anatase TiO_2, while it is −1.13 eV on the rutile TiO_2. Furthermore, the H adsorption energy ($E(H_{ads})$) on rutile and anatase was calculated to be −1.40 eV and 0.21 eV, respectively. This result indicates that H adsorption on rutile is very stable, making it eventually impossible to be desorbed from the rutile TiO_2 surface. In comparison, H adsorption on anatase TiO_2 is moderately endothermic, which can be easily overcome by external stimulation (such as light excitation) to enable process (1). Meanwhile, the small Gibbs free energy also facilitates the H desorption process.

The H adsorption/desorption behaviour is significant for the continuous conversion of CH_4. Although process (1) is important for CH_4 activation, the H desorption is critical in clearing the TiO_2 surface and allowing continuous CH_4 activation. The dramatic negative Gibbs free energy on rutile makes process (1) irreversible, terminating the CH_4 activation process, whereas process (1) on anatase is reversible, enabling the continuous CH_4 conversion. To further investigate the H desorption feature, temperature-programmed desorption mass spectrometry of CH_4 (TPD-MS-CH_4) experiments were carried out. An obvious H_2 molecular signal in Fig. 4c indicates the cleavage of CH_4 molecules on the catalyst. Moreover, the rutile phase TiO_2 shows much higher H_2 desorption temperatures than the anatase phase, indicating a stronger H bonding energy on rutile TiO_2. Fig. 4d schematically explains the difference in CH_4 activation on rutile and anatase surfaces. On the rutile surface, strong bonding between hydrogen atoms and surface sites leads to higher energy barriers for desorption, whereas on the anatase surface, weaker interactions facilitate desorption more easily. This variation in desorption capability can significantly tune the PMC performance.

In conclusion, we demonstrated that the rutile TiO_2 surface is inert during CH_4 activation, and the influence of surface CH_4 adsorption can outweigh the CST improvement when a phase junction is formed between anatase and rutile. Further investigation on CH_4 activation reveals the significant impact of the H-adsorption/desorption process during C–H bond breaking. A reversible H-adsorption/desorption with a small Gibbs free energy not only enables the activation of the first C–H bond in CH_4 but also ensures the removal of surface adsorbed species to facilitate the continuous process of photocatalytic CH_4 conversion. This research highlights the critical role of H desorption for continuous CH_4 activation and provides a new understanding of the design of efficient photocatalysts for methane conversion to produce value-added chemicals.

Data availability

The data supporting this article have been included as part of the ESI.†

Author contributions

L. W. and Z. W. proposed the research direction, designed the project, and guided the project. J. Y., L. W., and Z. W. designed various experiments. A. B. performed the theoretical calculation. J. Y., D. Y., Y. Z., and S. D. performed the experiments (synthesis, characterisations, catalysis, mechanism) and analysed the data. The overall manuscript was written by J. Y. and Z. W. Everyone commented on the manuscript. G. Z., Y. J., and J. H. participated in editing the manuscript.

Conflicts of interest

There are no conflicts to declare.

Acknowledgements

The authors would like to acknowledge the support from the Australian Research Council through its Future Fellowship (FT230100251), DECRA (DE210100930), Discovery (DP200101900) and Laureate Fellowship (FL190100139) schemes. This work used the Queensland node of the NCRIS-enabled Australian National Fabrication Facility (ANFF). This work was performed in part at the Queensland node of the Australian National Fabrication Facility, a company established under the National Collaborative Research Infrastructure Strategy to provide nano- and microfabrication facilities for Australia's researchers. The authors acknowledge the facilities and the scientific and technical assistance of the Australian Microscopy and Microanalysis Research Facility at the Centre for Microscopy and Microanalysis, The University of Queensland. The authors acknowledge access to computational resources at the NCI National Facility through the National Computational Merit Allocation Scheme supported by the Australian Government. This research was undertaken on the PD beamline at the Australian Synchrotron, part of ANSTO. J. Y. acknowledges scholarship support from UQ Graduate School.

References

1 S. Shoji, X. Peng, A. Yamaguchi, R. Watanabe, C. Fukuhara, Y. Cho, T. Yamamoto, S. Matsumura, M.-W. Yu, S. Ishii, T. Fujita, H. Abe and M. Miyauchi, *Nat. Catal.*, 2020, **3**, 148–153.
2 Z. Liu, B. Xu, Y.-J. Jiang, Y. Zhou, X. Sun, Y. Wang and W. Zhu, *ACS Environ. Au*, 2023, **3**, 252–276.
3 Q. Li, Y. Ouyang, H. Li, L. Wang and J. Zeng, *Angew. Chem., Int. Ed.*, 2022, **61**, e202108069.
4 X. Li, C. Wang and J. Tang, *Nat. Rev. Mater.*, 2022, **7**, 617–632.
5 J. F. Kasting, K. J. Zahnle and J. C. G. Walker, *Precambrian Res.*, 1983, **20**, 121–148.
6 J. You, Y. Bao, Y. Zhang, M. Konarova, Z. Wang and L. Wang, *EES Catal.*, 2024, **2**, 1210–1227.
7 J. Schneider, M. Matsuoka, M. Takeuchi, J. Zhang, Y. Horiuchi, M. Anpo and D. W. Bahnemann, *Chem. Rev.*, 2014, **114**, 9919–9986.
8 A. Kudo and Y. Miseki, *Chem. Soc. Rev.*, 2009, **38**, 253–278.
9 W. Cao, W. Zhang, L. Dong, Z. Ma, J. Xu, X. Gu and Z. Chen, *Exploration*, 2023, **3**, 20220169.
10 Y. Jiang, Y. Fan, S. Li and Z. Tang, *CCS Chem.*, 2023, **5**, 30–54.
11 X.-Y. Lin, J.-Y. Li, M.-Y. Qi, Z.-R. Tang and Y.-J. Xu, *Catal. Commun.*, 2021, **159**, 106346.
12 S. Murcia-López, K. Villa, T. Andreu and J. R. Morante, *ACS Catal.*, 2014, **4**, 3013–3019.
13 Z. Zhu, W. Guo, Y. Zhang, C. Pan, J. Xu, Y. Zhu and Y. Lou, *Carbon Energy*, 2021, **3**, 519–540.
14 S. Dutta, J. E. Erchinger, F. Strieth-Kalthoff, R. Kleinmans and F. Glorius, *Chem. Soc. Rev.*, 2024, **53**, 1068–1089.
15 R. Qian, H. Zong, J. Schneider, G. Zhou, T. Zhao, Y. Li, J. Yang, D. W. Bahnemann and J. H. Pan, *Catal. Today*, 2019, **335**, 78–90.
16 S. Zhu and D. Wang, *Adv. Energy Mater.*, 2017, **7**, 1700841.
17 Y. Ma, X. Wang, Y. Jia, X. Chen, H. Han and C. Li, *Chem. Rev.*, 2014, **114**, 9987–10043.
18 P. Zhou, I. A. Navid, Y. Ma, Y. Xiao, P. Wang, Z. Ye, B. Zhou, K. Sun and Z. Mi, *Nature*, 2023, **613**, 66–70.
19 Q. Wang and K. Domen, *Chem. Rev.*, 2020, **120**, 919–985.
20 Z. Wang, Y. Gu, L. Zheng, J. Hou, H. Zheng, S. Sun and L. Wang, *Adv. Mater.*, 2022, **34**, 2106776.
21 Y. Qi, S. Chen, J. Cui, Z. Wang, F. Zhang and C. Li, *Appl. Catal., B*, 2018, **224**, 579–585.
22 C. Cheng, B. He, J. Fan, B. Cheng, S. Cao and J. Yu, *Adv. Mater.*, 2021, **33**, 2100317.
23 M. Sachs, R. S. Sprick, D. Pearce, S. A. J. Hillman, A. Monti, A. A. Y. Guilbert, N. J. Brownbill, S. Dimitrov, X. Shi, F. Blanc, M. A. Zwijnenburg, J. Nelson, J. R. Durrant and A. I. Cooper, *Nat. Commun.*, 2018, **9**, 4968.
24 S. Odabasi Lee, S. K. Lakhera and K. Yong, *Adv. Energy Sustainability Res.*, 2023, **4**, 2300130.
25 R. Yanagi, T. Zhao, D. Solanki, Z. Pan and S. Hu, *ACS Energy Lett.*, 2022, **7**, 432–452.
26 Y. Jiang, S. Li, Y. Fan and Z. Tang, *Angew. Chem., Int. Ed.*, 2024, **63**, e202404658.
27 X. Guo, G. Fang, G. Li, H. Ma, H. Fan, L. Yu, C. Ma, X. Wu, D. Deng, M. Wei, D. Tan, R. Si, S. Zhang, J. Li, L. Sun, Z. Tang, X. Pan and X. Bao, *Science*, 2014, **344**, 616–619.
28 X. Meng, X. Cui, N. P. Rajan, L. Yu, D. Deng and X. Bao, *Chem*, 2019, **5**, 2296–2325.
29 P. Schwach, X. Pan and X. Bao, *Chem. Rev.*, 2017, **117**, 8497–8520.
30 A. I. Olivos-Suarez, À. Szécsényi, E. J. M. Hensen, J. Ruiz-Martinez, E. A. Pidko and J. Gascon, *ACS Catal.*, 2016, **6**, 2965–2981.
31 S. Song, H. Song, L. Li, S. Wang, W. Chu, K. Peng, X. Meng, Q. Wang, B. Deng, Q. Liu, Z. Wang, Y. Weng, H. Hu, H. Lin, T. Kako and J. Ye, *Nat. Catal.*, 2021, **4**, 1032–1042.
32 P. Wang, R. Shi, Y. Zhao, Z. Li, J. Zhao, J. Zhao, G. I. N. Waterhouse, L.-Z. Wu and T. Zhang, *Angew. Chem., Int. Ed.*, 2023, **62**, e202304301.
33 M. Xiao, L. Wang, H. Wang, J. Yuan, X. Chen, Z. Zhang, X. Fu and W. Dai, *Catal. Sci. Technol.*, 2023, **13**, 4148–4155.
34 J. Lang, Y. Ma, X. Wu, Y. Jiang and Y. H. Hu, *Green Chem.*, 2020, **22**, 4669–4675.
35 W. Zhang, C. Fu, J. Low, D. Duan, J. Ma, W. Jiang, Y. Chen, H. Liu, Z. Qi, R. Long, Y. Yao, X. Li, H. Zhang, Z. Liu, J. Yang, Z. Zou and Y. Xiong, *Nat. Commun.*, 2022, **13**, 2806.
36 X. Li, J. Xie, H. Rao, C. Wang and J. Tang, *Angew. Chem., Int. Ed.*, 2020, **59**, 19702–19707.
37 X. Li, C. Wang, J. Yang, Y. Xu, Y. Yang, J. Yu, J. J. Delgado, N. Martsinovich, X. Sun, X.-S. Zheng, W. Huang and J. Tang, *Nat. Commun.*, 2023, **14**, 6343.
38 X. Li, C. Li, Y. Xu, Q. Liu, M. Bahri, L. Zhang, N. D. Browning, A. J. Cowan and J. Tang, *Nat. Energy*, 2023, **8**, 1013–1022.
39 R. Li, Y. Weng, X. Zhou, X. Wang, Y. Mi, R. Chong, H. Han and C. Li, *Energy Environ. Sci.*, 2015, **8**, 2377–2382.
40 R. Abe, K. Sayama and H. Sugihara, *J. Phys. Chem. B*, 2005, **109**, 16052–16061.
41 K. Maeda, *Chem. Commun.*, 2013, **49**, 8404–8406.

42 K. Maeda and K. Domen, *J. Phys. Chem. Lett.*, 2010, **1**, 2655–2661.

43 W. Kim, T. Tachikawa, G.-h. Moon, T. Majima and W. Choi, *Angew. Chem., Int. Ed.*, 2014, **53**, 14036–14041.

44 Y. Ma, X. Wang and C. Li, *Chin. J. Catal.*, 2015, **36**, 1519–1527.

45 D. C. Hurum, A. G. Agrios, K. A. Gray, T. Rajh and M. C. Thurnauer, *J. Phys. Chem. B*, 2003, **107**, 4545–4549.

46 J. Chen, T. Chen, Q. Fang, C. Pan, O. U. Akakuru, W. Ren, J. Lin, A. Sheng, X. Ma and A. Wu, *Exploration*, 2022, **2**, 20220014.

47 N. Feng, H. Lin, H. Song, L. Yang, D. Tang, F. Deng and J. Ye, *Nat. Commun.*, 2021, **12**, 4652.

48 Y. Jiang, W. Zhao, S. Li, S. Wang, Y. Fan, F. Wang, X. Qiu, Y. Zhu, Y. Zhang, C. Long and Z. Tang, *J. Am. Chem. Soc.*, 2022, **144**, 15977–15987.

49 W.-K. Wang, J.-J. Chen, X. Zhang, Y.-X. Huang, W.-W. Li and H.-Q. Yu, *Sci. Rep.*, 2016, **6**, 20491.

50 C. R. Aita, *Appl. Phys. Lett.*, 2007, **90**(21), 213112.

51 W. F. Zhang, Y. L. He, M. S. Zhang, Z. Yin and Q. Chen, *J. Phys. D: Appl. Phys.*, 2000, **33**, 912.

52 D. Hu, C. Dong, S. Belhout, S. Shetty, H. Ng, P. Brasseur, L. S. Bezerra, K. Ben Tayeb, P. Simon, A. Addad, M. Virginie, R. Wojcieszak, V. V. Ordomsky, P. H. C. Camargo and A. Y. Khodakov, *Mater. Today Energy*, 2023, **36**, 101358.

53 J. You, M. Xiao, S. Liu, H. Lu, P. Chen, Z. Jiang, W. Shangguan, Z. Wang and L. Wang, *J. Mater. Chem. A*, 2023, **11**, 10149–10154.

54 Y. Zhang, D. Yao, B. Xia, M. Jaroniec, J. Ran and S.-Z. Qiao, *ACS Energy Lett.*, 2022, **7**, 1611–1617.

55 J. Zhang, M. Li, Z. Feng, J. Chen and C. Li, *J. Phys. Chem. B*, 2006, **110**, 927–935.

56 J. Zhang, Q. Xu, M. Li, Z. Feng and C. Li, *J. Phys. Chem. C*, 2009, **113**, 1698–1704.

57 D. O. Scanlon, C. W. Dunnill, J. Buckeridge, S. A. Shevlin, A. J. Logsdail, S. M. Woodley, C. R. A. Catlow, M. J. Powell, R. G. Palgrave, I. P. Parkin, G. W. Watson, T. W. Keal, P. Sherwood, A. Walsh and A. A. Sokol, *Nat. Mater.*, 2013, **12**, 798–801.

58 W. Liu, L. Cao, W. Cheng, Y. Cao, X. Liu, W. Zhang, X. Mou, L. Jin, X. Zheng, W. Che, Q. Liu, T. Yao and S. Wei, *Angew. Chem., Int. Ed.*, 2017, **56**, 9312–9317.

59 R. Li, T. Takata, B. Zhang, C. Feng, Q. Wu, C. Cui, Z. Zhang, K. Domen and Y. Li, *Angew. Chem., Int. Ed.*, 2023, **62**, e202313537.

60 G. Zhai, L. Cai, J. Ma, Y. Chen, Z. Liu, S. Si, D. Duan, S. Sang, J. Li, X. Wang, Y.-A. Liu, B. Qian, C. Liu, Y. Pan, N. Zhang, D. Liu, R. Long and Y. Xiong, *Sci. Adv.*, 2024, **10**, eado4390.

61 Z. Li, P. Chen, J. Feng, M. Zhao, Z. Zhao, Y. Zhang, X. Xu, H. Huang, Z. Zou and Z. Li, *Angew. Chem., Int. Ed.*, 2024, e202409876.

62 A. Ishikawa and Y. Tateyama, *ACS Catal.*, 2021, **11**, 2691–2700.

63 X. Wang, N. Luo and F. Wang, *Chin. J. Chem.*, 2022, **40**, 1492–1505.

64 Q. Zhan, Y. Kong, X. Wang and L. Li, *Chem. Commun.*, 2024, **60**, 2732–2743.

65 J. Zhang, J. Shen, D. Li, J. Long, X. Gao, W. Feng, S. Zhang, Z. Zhang, X. Wang and W. Yang, *ACS Catal.*, 2023, **13**, 2094–2105.

66 G. Liu, H. G. Yang, J. Pan, Y. Q. Yang, G. Q. Lu and H. M. Cheng, *Chem. Rev.*, 2014, **114**, 9559–9612.

67 Y. Chen, L. Soler, C. Cazorla, J. Oliveras, N. G. Bastús, V. F. Puntes and J. Llorca, *Nat. Commun.*, 2023, **14**, 6165.

68 L. Li, J. Yan, T. Wang, Z.-J. Zhao, J. Zhang, J. Gong and N. Guan, *Nat. Commun.*, 2015, **6**, 5881.